Segmentation of Pathology in Tumor-Diseased Brains

Lect. Mohammed Hatim Khdair
Computer and Software Engineering Department, College of Engineering
Al-Mustansiriya University, Baghdad, Iraq

Abstract

Automatic segmentation of multiple sclerosis lesions in magnetic resonance images remains a challenging task. In this study, we present a fully automatic method to extract lesions from multi-sequence MRI (T1, T2, T2 FLAIR, Proton Density) within an Expectation Maximization (EM) based probabilistic framework.

The method uses the available MRI sequences in a hierarchical, orderly manner. First the T2 FLAIR sequence is used to generate a segmentation of supra-tentorial lesions. Then T2 and T1 lesion loads are computed, providing an insight into lesion structure.

الخلاصـــــة

التصنيف الآلي لأذى تصلّبِ الأنسجة المتعدّدةِ في بقايا صورِ الرنينِ المغناطيسية هوَ تحدّي شاقّ. حيث تم في هذه الدراسةِ، تُقديّمُ طريقة آلية بالكامل لانتزاع الأذى مِنْ تصوير بالرّنين المغناطيسي متعدّدِ السلسلَة (T1, T2, T2 FLAIR, Proton Density) ضمن تحقيق حدّ توقّعِ الأقصى (EM) ذات إسناد إطار احتمالي.

حيث تَستعملُ هذه الطريقةُ سلاسلَ التصوير بالرّنين المغناطيسي والمرتبة بطريقة هرمية. أولاً سلسلة T2 FLAIR استخدمت لتوليد تصنيف الأذى السطحي. ثمّ T2 و T1 لأحمال الأذى المَحْسُوبة، والذي يسلط الضوء على تركيبِ الأذى.

1. Introduction

Magnetic Resonance Imaging (MRI) is the primary complementary exam for the monitoring and diagnosis of multiple sclerosis (MS) [1]. MS lesions exhibit hypersignals in T2 and hyposignals in T1, with respect to normal white matter intensities. Typically, lesions appear smaller in T1 than T2, reflecting their complex internal structure. T1 lesion load has already been successfully correlated with the Expanded Disability Status Scale (EDSS) using large sets of patients, while there is little evidence of the clinical relevance of T2 lesion load [2]. In any case, an automatic segmentation system that generates different quantifiers is useful for diagnosis and clinical trials [3].

Hyperintense signals in T2 images provide a good measure of the overall tissue injury [4]. However, since the intensities of lesions and cerebro-spinal fluid (CSF) are close, this may lead to misclassification. The T2 FLAIR sequence offers good contrast between MS lesions and CSF [5]. Even though it highlights supra-tentorial lesions mostly, it is known that using this sequence increases sensitivity and specificity for the case of MS lesion segmentation [6].

Existing multi-sequence MS lesion segmentation methods [7, 8, 9] give equal importance to the set of MRI sequences, which are employed all at once, ignoring their differences. Instead, we propose a hierarchical method that uses information in an orderly manner. We first consider the four sequences T1, T2, T2 FLAIR, Proton Density to build a mask of brain tissues, and segment them into three classes: white matter, grey matter, CSF. The parameters are then extracted to automatically compute a threshold that we apply on the T2 FLAIR sequence to get a mask of MS lesions. Finally, we can separate outliers from lesions and use this mask to aid in the segmentation of T1 data and the computation of lesion loads.

2. Segmentation of a Surgical Resection

A surgical resection corresponds to an absence of matter in the considered region, filled with CSF, and possibly connected with the ventricles. Its shape is more spherical than the other structures of the CSF, and is composed of only one big connected component. These are the basic properties that we exploit for delineating the resection.

First, we extract all structures behaving like CSF in the joint MR T1 and T2 histogram (low signal in T1 and high signal in T2) by fitting a 2D Gaussian on the corresponding area of the histogram. Selecting all the voxels whose joint intensity is statistically compatible gives us an oversized segmentation of CSF which still contains structures like the eyes and the ventricles. The eyes are quite easy to remove since they appear as two isolated connected components. To select them, we robustly register an atlas with an affine transformation, and remove the connected components that have an intersection with the eyes of the atlas. To separate the ventricles from the surgical resection, we use a region labeling algorithm based on a skeletonization by influence zone (SKIZ) Soille (1999). As this labeling is sensitive to narrowings in a connected component, it easily classifies the surgical resection and the

ventricle as different regions. The regions that intersect the ventricles of the atlas are removed as above.

Finally, we have to select the surgical resection region among remaining structures. The sulci are relatively small with respect to a surgical resection and thus easy to remove. The main problem comes from the possible presence of a CSF component between the brain and the skull due to brain shift during the surgical operation. The volume of this component may be quite large, but its shape is mostly flat. Thus, we compute a distance map in each remaining CSF connected component, and select the one that has the largest inscribed ball radius.

3. Delineation of the Tumor

Delineating a tumor is a hard task due to the multiple appearances it may have in the image. The tumor may generate an edema at its frontiers, and contain a necrotic center. The tumor tissues and the edema usually appear like partial volume (CSF and grey matter) intensities, while the necrosis resembles the CSF.

Traditional Expectation-Maximization algorithms (Leemput et. al. (1999)) fail to provide good results because of the presence of these tissues. An alternative is to consider tumor intensities as outliers in this mixture of Gaussians, or to add some specific classes to model the tumor and edema intensities (Moon et. al. (2002)). As this was often not sufficient, some anatomical knowledge was added, either by combining geometric priors given by the non-rigid registration of an atlas to a tissue classification (Kaus et. al. (2001)), or by using Markov Random Fields (Kapur (1999)). Other methods include region growing from a region of interest delineated by one of the preceding methods using level-sets methods (Ho et. al. (2002)).

All these methods end up in very complex algorithm as they attempt to segment all the tissues. In our case, we are only interested in the tumor segmentation, so that we could rely on a very simple mathematical morphology scheme as we developed in the previous section.

We fit this time a mixture of two Gaussians to the selected region of the joint T1 a T2 intensity histogram: one for the necrotic part of the tumor (which appear like CSF), and a second one for the tumor tissues and its edema (resembling partial volume CSF/grey matter). We obtain an oversized segmentation where we need to remove structures like the sulci or the ventricles without removing interesting parts. Indeed, we now have CSF and grey matter partial volume voxels, and the necrotic part of the tumor can be near a region containing CSF. The ventricles and the eyes are removed like before. Then the remaining part of the segmentation is labeled into SKIZ zones. Each region is then compared with an a priori statistical atlas of the CSF to compute the mean probability of belonging to the CSF. A threshold on this probability allows us to remove the CSF structures like the ventricles or the sulci. In each of these two steps we also compute a distance map to the CSF of the statistical atlas in each region to avoid removing regions containing voxels too far from the expected CSF.

3-1 The Registration of Brain MRI's from Parkinsonian Patients

We tested our algorithm by registering 10 3D T1-weighted MRI images of Parkinsonian patients, such as the ones presented in **Fig.(1)**. They were all acquired using the IR-FSPGR (3D acquisition, Inversion Recovery, Fast Spoiled Gradient Echo) protocol and field strength of 1.5T. These images were acquired preoperatively under stereotactic conditions, in order to select optimal targets for deep brain stimulation. All images have the same sizes $256\times256\times124$. In order to eliminate large displacements that do not reflect anatomical differences, image couples were affinely registered before the non-rigid registration.

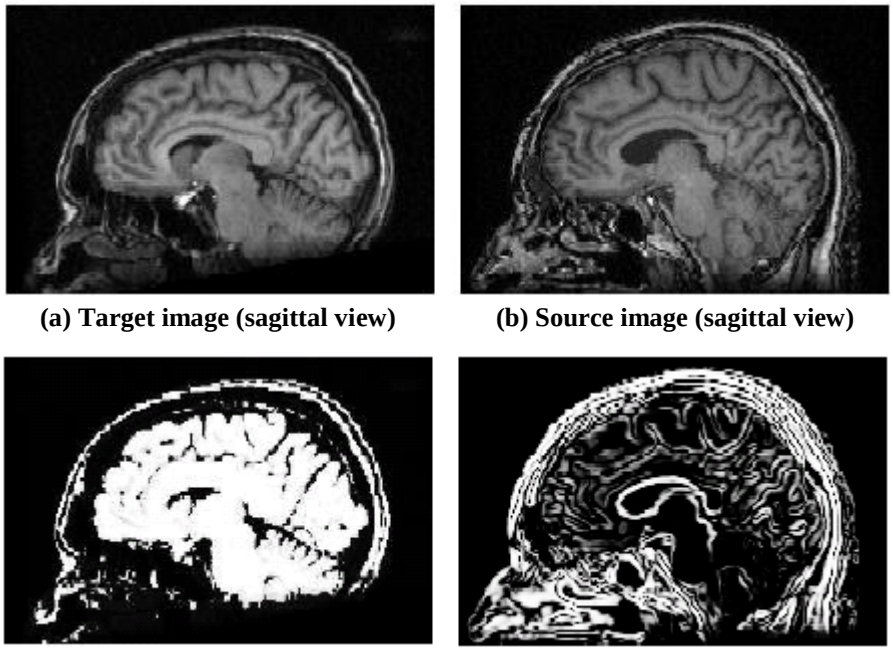

(a) Target image (sagittal view) **(b) Source image (sagittal view)**

(c) Stiffness information **(d) Confidence**

Figure (1) Registering two T1-MRI images of different subjects
The four images present the same sagittal slice of the target and source images, and the stiffness and confidence fields. The images are courtesy of Pr. D. Dormont (Neuro-radiology Dept., Pitié-Salpétrière Hospital, Paris, France)

3-1-1 Parameter Tuning

3-1-1-1 Confidence Field

We compute the confidence as a function of source image gradient, as described by Equation (1) below. The values of c and λ are parameters of the algorithm (the way to tune their values is detailed below in this section). **Fig.(1d)** presents a slice of the computed confidence field (k). Its values give the amount of smoothing of the incremental correction field. In places where these values are low, the correction field will be smoother (remark that the diffusion is weighted by $1-k$), there by making these regions count less in the registration. At each iteration, the confidence field is resampled into the deformed geometry.

$$k(p) = \exp\left(\frac{-c}{\left(\frac{\|\nabla J(p)\|}{\lambda}\right)^4}\right) \quad \text{..... (1)}$$

The confidence described in the above equations is close to 1 for large image gradients, and to 0 in uniform areas. λ is a contrast parameter that discriminates low contrast regions (which are mainly diffused) from high contrast ones (which preserve the edges in the deformation field), and c is a scalar parameter usually taken around 3.3 (see Weickert (2000)).

3-1-1-2 Stiffness Field

In brain images, the shapes of structures like ventricles or gyri are highly varying. A common problem with non-rigid registration algorithms that use a uniform regularization is their inability to properly deform the ventricles. In our algorithm, the regularization allows the use of a higher level of regularization in certain areas than in others. For choosing the local level of regularization inside a structure, a good reference would be the relative variability of the structure (normalized by its size). Computing such a measure is a difficult problem. Our experience showed that a good choice is to use a level of regularization three times larger within the brain than in the fluid-dominated areas (inside the cerebro-spinal fluid and image background). Achieving a fuzzy segmentation of these areas for T1-MRI images of healthy subjects is rather straightforward, since a simple thresholding gives rather good results. However, we wanted a more general segmentation method, able to take into account other modalities, and also brains with pathologies. Thus, we considered classification algorithms.

In these experiments, we used the fuzzy k-means algorithm (Bezdek (1981); de-Gruijter and McBratney (1988)) to classify the images into five classes: image background, cerebro-spinal fluid (CSF), grey matter (GM), white matter (WM) and fat. If $P_{back}(p), P_{csf}(p), P_{gm}(p), P_{wm}(p), and\ P_{fat}(p)$ are the fuzzy memberships at a voxel p for respectively, the image background, CSF, grey matter, white matter and fat classes, we compute the stiffness field (**Fig.(1c)**) as:

$$d(p) = P_{gm}(p) + P_{wm}(p) + P_{fat}(p) \quad \text{..... (2)}$$

As an input, the classification algorithm needs initial estimates of the average values of the classes. These protocol parameters are easily specified by the user: thanks to the graphical interface we have developed, the user visualizes the images and interactively determines the initial intensity values for each tissue class. They are used as input parameters (five for each image to register) of the fuzzy k-means algorithm.

3-1-1-3 Time Steps

The result of the registration depends on the similarity gradient descent fraction $\in$, the two diffusion (elastic and fluid) time steps, and the parameters c and λ from Equation (1). Manually tuning these parameters can be a tedious task, since regularization and similarity have different units. Our solution is to provide a normalization of the intensities before registration, as follows: From the fuzzy segmentation that allowed us to compute the stiffness field, we take the average intensity of the white matter μ_{wm} as a reference level, and then apply the following intensity correction:

$I_{new} = \frac{K}{\mu_{wm}} I_{old}$, where K is a known constant giving the final intensities.

We have experimentally noticed that the normalization procedure described below for T1-MRI brain images significantly decreases the sensitivity of the algorithm with respect to these parameters. Once the algorithm parameters are tuned for a certain value of K, the user does not have to change their values significantly between two experiments. In fact, all the experiments presented in this section were done using the same values of the parameters (K = 256, c = 3:3, λ = 300, Δt = 0:3, $\in$ = 0:0006).

4. Results and Discussion

The algorithm was run in parallel on a cluster of 3GHz Pentium IV personal computers, linked together through a 0.5GB/s Ethernet network. For these images of size $256 \times 256 \times 124$, the computation time was 10 minutes, 38 seconds. For comparison, the same registration on a single machine takes 1 hour. **Figure (2)** presents a first registration experiment: large anatomical differences are well recovered by the algorithm, while keeping the transformation invertible and smooth.

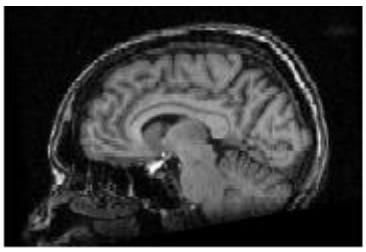

(a) Target image (sagittal view)

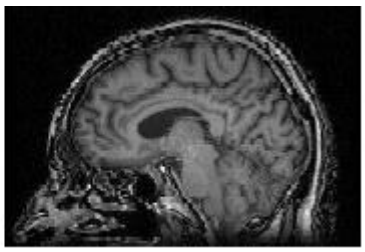

(b) Source image (sagittal view)

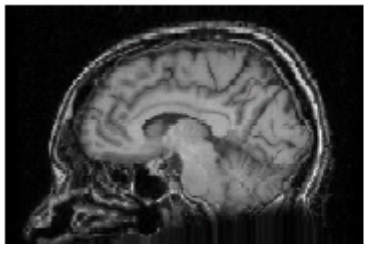

(c) Resampled source image after registration (compare to image in Fig. a)

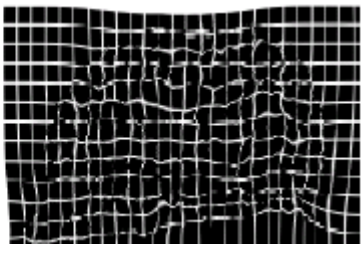

(d) The deformation field (applied to a regular grid)

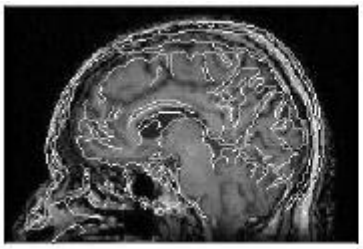

(e) Target contours, superimposed on the source image before registration

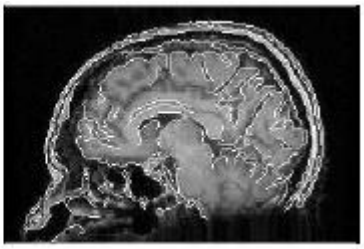

(f) Target contours, superimposed on the resampled source image after registration

Figure (2) Registration experiment: Even if the brains presented in the source (Fig. b) and target (Fig. a) images are anatomically rather different, the resampled image after registration (Fig. c) is very close to the target image (Fig. a). The algorithm is able to recover very well the shapes of the ventricles and the major sulci. The recovered displacement field (Fig. d) is smooth. The differences are also presented by superposing contours from the target on the source and resampled images (see, respectively, Fig. e and f)

Figures (3) and **(4)** present a second and third experiment, using images of different patients. The result in **Fig.(3)** is remarkable in the fact that the algorithm was able to successfully recover the very large difference that exists in the shape of the ventricles.

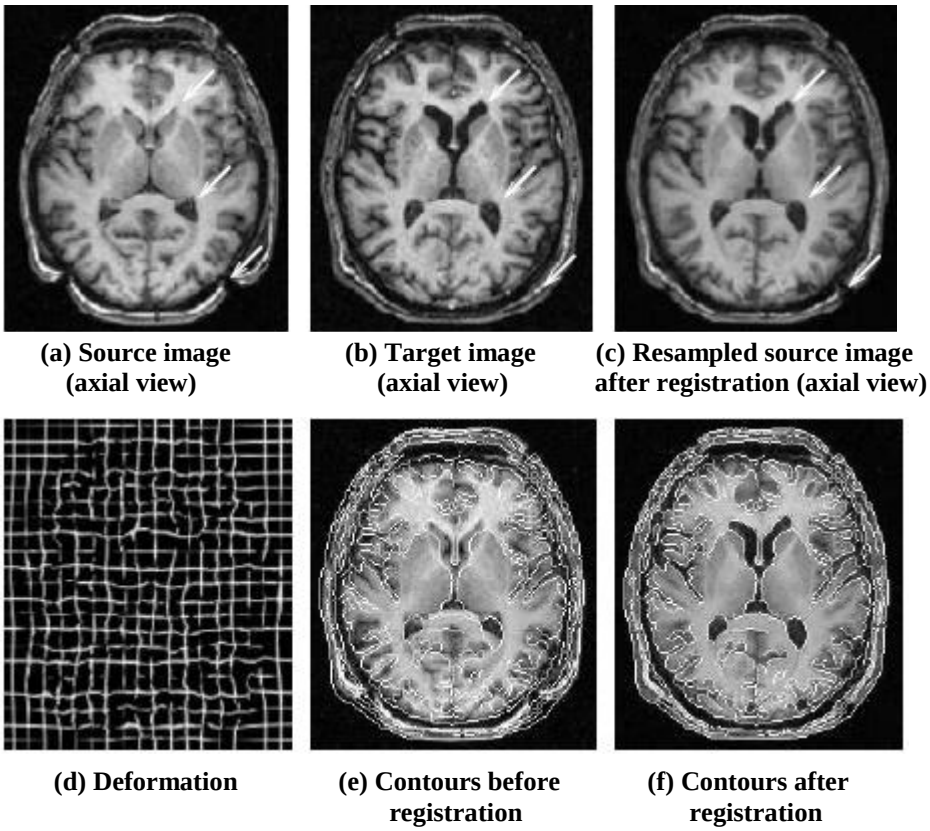

(a) Source image (axial view) **(b) Target image (axial view)** **(c) Resampled source image after registration (axial view)**

(d) Deformation **(e) Contours before registration** **(f) Contours after registration**

Figure (3) Second experiment. The figures show the same axial view for all images

The upper and middle white arrows underline two parts of the ventricles where the source and target images are particularly different. The lower white arrow points to a hole in the skull skin in the source image (Fig. a). This hole is caused by surgery and is not present in the target image (Fig. b). However, after registration, the hole was preserved in the resampled image (Fig. c). We believe that this is the right behavior, since the hole can be consider a part of the image anatomy. The transformation (Fig. d) is invertible and smooth. Figures e and f allow to examine more closely the quality of the result, by comparing target contours superposed on the source image before and after registration (Fig. e and f)

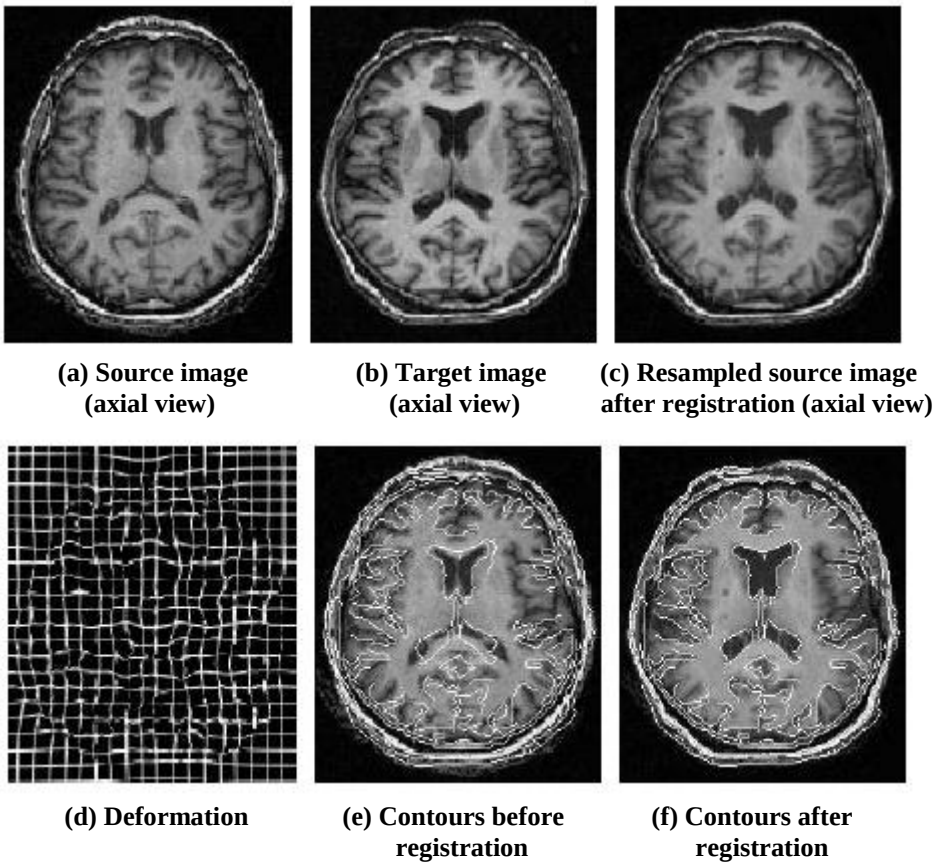

(a) Source image (axial view) **(b) Target image (axial view)** **(c) Resampled source image after registration (axial view)**

(d) Deformation **(e) Contours before registration** **(f) Contours after registration**

Figure (4) Third experiment: The algorithm is able to compensate very large variations of the shape of the ventricles
The resampled image (Fig. c) is very close to the target image (Fig. b), despite very large initial anatomical differences (Fig. e). The transformation is smooth and invertible (Fig. d)

5. Conclusion

When attempting to segment real patient images by registering them with an anatomical atlas for radiotherapy planning, we encountered the following problem: the tumor or the possible surgical resection present in the patient image has no correspondent in the atlas. Therefore, false correspondences are estimated for points inside the pathology, which leads to a locally erroneous registration. The solution described in "Pathology-aware registration for 3D conformal radiotherapy planning" consists in giving the pathological voxels a low weight in the registration. Results show that this tends to interpolate the displacement field inside the tumor from its values outside it, which prevents potential distortions caused by the pathology.

6. References

1. A., Tourbah, ***"IRM Et Scl´erose En Plaques"***, Neurologies, Vol. 4, No. 33, 2001, pp. 270-274.

2. J., Grimaud, Y.-M., Zhu, and M., Rombaut, ***"Mise Au Point: Les Techniques D'analyse Quantitative Des IRM C´er´ebrales: Application `a la Scl´erose En Plaque"***, Revue Neurologique, Vol. 158, No. 3, 2002, pp. 381-389.

3. E. M., Frohman, D. S., Goodin, P. A., Calabresi, J. R., Corboy, P. K., Coyle, M., Filippi, J. A., Frank, S. L., Galetta, R. I., Grossman, K., Hawker, N. J., Kachuck, M. C., Levin, J. T., Phillips, M. K., Racke, V. M., Rivera, and W. H., Stuart, ***"The Utility of MRI in Suspected MS: Report of the Therapeutics and Technology Assessment Subcommittee of the American Academy of Neurology"***, Neurology, Vol. 61, No. 5, 2003, pp. 602-11.

4. M., Filippi, and R. I., Grossman, ***"MRI Techniques to Monitor MS Evolution: The Present and the Future"***, Neurology, Vol. 58, No. 8, 2002, pp. 1147-1153.

5. I. L., Tan, R. A., Van Schijndel, P. J., Pouwels, H. J., Ader, and F., Barkhof, ***"Serial Isotropic Three-Dimensional Fast FLAIR Imaging: Using Image Registration and Subtraction to Reveal Active Multiple Sclerosis Lesions"***, AJR Am J Roentgenol, Vol. 179, No. 3, 2002, pp. 777-82.

6. E. H., Herskovits, R., Itoh, and E. R., Melhem, ***"Accuracy for Detection of Simulated Lesions: Comparison of Fluid-Attenuated Inversion-Recovery, Proton Density-Weighted, and T2-Weighted Synthetic Brain MR Imaging"***, AJR Am J Roentgenol, Vol. 176, No. 5, 2001, pp. 1313- 8.